NeuroImage 262 (2022) 119559

Contents lists available at ScienceDirect

NeuroImage

journal homepage: www.elsevier.com/locate/neuroimage

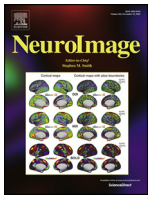

Cross-Axis Dynamic Field Compensation of Optically Pumped Magnetometer Arrays for MEG

Stephen E. Robinson[1,*], Amaia Benitez Andonegui[1], Tom Holroyd[1], K. Jeramy Hughes[2,3], Orang Alem[2,3], Svenja Knappe[2,3], Tyler Maydew[2], Andreas Griesshammer[2], Allison Nugent[1]

[1] MEG Core Facility, NIMH/NIH, Bethesda, MD
[2] FieldLine Inc., Boulder, CO
[3] University of Colorado Boulder, Boulder, CO

ARTICLE INFO

Key words:
Optically pumped magnetometer
Magnetoencephalography
Linearity
Cross-axis projection error
Dynamic field compensation
Synthetic gradiometer

ABSTRACT

We present dynamic field compensation (DFC), whereby three-axis field measurements from reference magnetometers are used to dynamically maintain null at the alkali vapor cells of an array of primary sensors that are proximal to a subject's scalp. Precision measurement of the magnetoencephalogram (MEG) by zero-field optically pumped magnetometer (OPM) sensors requires that sensor response is linear and sensor gain is constant over time. OPMs can be operated in open-loop mode, where the measured field is proportional to the output at the demodulated photodiode output, or in closed-loop, where on-board coils are dynamically driven to maintain the internal cell at zero field in the measurement direction. While OPMs can be operated in closed-loop mode along all three axes, this can increase sensor noise and poses engineering challenges. Uncompensated fluctuations in the ambient field along any statically nulled axes perturb the measured field by tipping the measurement axis and altering effective sensor gain – a phenomenon recently referred to as cross-axis projection error (CAPE). These errors are particularly problematic when OPMs are allowed to move in the remnant background field. Sensor gain-errors, if not mitigated, preclude precision measurements with OPMs operating in the presence of ambient field fluctuations within a typical MEG laboratory. In this manuscript, we present the cross-axis dynamic field compensation (DFC) method for maintaining zero field dynamically on all three axes of each sensor in an array of OPMs. Together, DFC and closed-loop operation strongly attenuate errors introduced by CAPE. This method was implemented by using three orthogonal reference sensors together with OPM electronics that permit driving each sensor's transverse field coils dynamically to maintain null field across its OPM measurement cell. These reference sensors can also be used for synthesizing 1st-gradient response to further reduce the effects of fluctuating ambient fields on measured brain activity and compensate for movement within a uniform field. We demonstrate that, using the DFC method, magnetic field measurement errors of less than 0.7% are easily achieved for an array of OPM sensors in the presence of ambient field perturbations of several nT.

1. Introduction

Evidence for the human magnetoencephalogram (MEG) alpha rhythm was first observed in 1968 by Cohen, using an inductive pickup coil (Cohen, 1968) and subsequently using a point-contact rf-SQUID (superconducting quantum interference device) magnetometer (Cohen, 1972). MEG became practical with the advent of multi-sensor whole-head instruments, using the more sensitive dc-SQUIDs to measure brain activity simultaneously from multiple sites (Ahonen et al., 1992; Cheyne et al., 1992; Fife et al., 2002). This enabled localization and imaging of focal brain activity (Hamalainen et al., 1993; Vrba and Robinson, 2000, 2002). The sensitivity and resolution of brain activity for commercially available dc-SQUID-based MEG sensors is limited by a liquid helium dewar vacuum gap of ~15 mm required to insulate the sensors operating at 4.2 K. The gap between these sensors and the scalp may be greater than 30 mm because the shape of the outer dewar surface is designed to accommodate at least 95% of head sizes. Smaller vacuum gaps of 1-3 mm are feasible for high-Tc dc-SQUID sensors, operating at ~70 K (Pfeiffer et al., 2020). Recently, optically pumped magnetometers (OPMs) with sufficient sensitivity for MEG measurements (~15 fT/$\sqrt{\text{Hz}}$) have been developed (Allred et al., 2002; Xia et al., 2006) and manufactured in compact sensor housings (Knappe et al., 2012; Shah and Wakai, 2013). Unlike low-Tc SQUID sensors, OPMs can be

* Corresponding author. Stephen E. Robinson, MEG Core Facility, National Institute of Mental Health, Magnussen Clinical Center, Room 2D49, MSC 1515, Bethesda, Maryland, USA. Phone: (301) 496-6886
E-mail address: robinsonse@mail.nih.gov (S.E. Robinson).

https://doi.org/10.1016/j.neuroimage.2022.119559.
Received 3 June 2022; Received in revised form 8 August 2022; Accepted 11 August 2022
Available online 13 August 2022.

located directly on the scalp, with a standoff of ~5 mm to the sensing cell. This increases signal-to-noise ratio (SNR) and sensitivity to higher magnetic field spatial frequencies (Boto et al., 2017; Iivanainen et al., 2021; Luessi et al., 2014; Riaz et al., 2017).

The current generation of commercially available OPM sensors employs a transparent heated vapor cell containing an alkali-metal vapor such as ^{87}Rb to detect the magnetic field. They are designed to operate in zero field under the spin-exchange relaxation-free (SERF) condition (Happer and Tang, 1973; Kim et al., 2014). The atoms in the vapor are spin-polarized using a pump laser tuned to the D1 spectral absorption line. The optical transparency of the vapor is a measure of the local magnetic field and is monitored by an internal photodetector (Dupont-Roc et al., 1969; Shah et al., 2007). The SERF OPM response to field change has the shape of an absorptive Lorentzian centered around zero magnetic field. Modulation and lock-in detection linearizes the dispersion curve in the vicinity of zero field and establishes the sensing axis (Allred et al., 2002; Dupont-Roc et al., 1969). Given that the sensor response is nonlinear outside a relatively narrow range (±2 nT), OPMs must be operated in a low field environment such as a magnetically shielded room (MSR) (Cohen, 1967). The static field within our typical commercial MSR is 30-40 nT with gradients of ~10 nT/m and low-frequency fluctuations are typically ~1-2 nT peak-to-peak. To ensure that the sensors are within the linear operating range, in open-loop operation the field within individual OPM sensors is nulled before measurement by means of three orthogonal sets of field coils surrounding the vapor cell. Because this static nulling process cannot correct for dynamic changes in field, due either to environmental fluctuations or movement of the array in the ambient field, additional solutions must be sought. The ambient magnetic field surrounding an OPM MEG sensor array can be reduced further using three orthogonal large field coils surrounding the subject's head (Iivanainen et al., 2019) or using a set of multilayer biplanar coils (MuCoils, Magnetic Shields Ltd, Kent, UK) to control fields and gradients without restricting subject access. The biplanar coils compensate three magnetic field and three of five first gradient (Holmes et al., 2019) components to yield a ± 5% field homogeneity within a 40 × 40 × 40 cm^3 volume enclosing the subject's head, reducing the field to within ±2 nT (Holmes et al., 2018; Holmes et al., 2019; Mellor et al., 2022; Mellor et al., 2021). While dynamic control of the MuCoils is possible (Hill et al., 2022; Holmes et al., 2019; Mellor et al., 2022), the remnant field combined with subject movement may nonetheless introduce fields exceeding the linear range of sensors operating in default open-loop mode. In addition to linearity errors induced by large field offsets, it has recently been reported that additional measurement errors are induced by small transverse ambient field offsets that perturb the sensing axis (Cohen-Tannoudji et al., 1970); this phenomenon has been referred to as cross-axis projection error (CAPE) (Borna et al., 2021). CAPE introduces both phase errors and a tilt of the sensing axis. At low frequencies this axis tilt is approximately 3.3°/nT (Borna et al., 2021). Offsets as small as ±1.5 nT result in effective gain errors of ~5 percent (Boto et al., 2018).

One solution to expand the range of linear operation of OPM sensors is to utilize closed-loop operation, in which negative feedback is applied dynamically to the measurement-axis field coils, thus maintaining zero field. In closed-loop mode the instantaneous field measurement is linearly proportional to the feedback current applied to the coils (Lee et al., 2014; Nardelli et al., 2020). While closed-loop operation in the sensing direction improves the linearity of the sensor response, it does not mitigate CAPE due to transverse field offsets. Thus, while non-linearities in the sensor response due to the inherent shape of the dispersion curve are reduced, significant measurement errors are induced when fields are present in the transverse directions due either to errors in the static nulling of the field, changes in the ambient field, or movement. A potential solution for mitigating CAPE is operation of the OPMs in closed-loop mode on all three axes. Although triaxial OPM sensors have been fabricated (Huang et al., 2015; Yan et al., 2022), there are currently no commercially available triaxial sensors employing closed-loop operation on all three axes. Furthermore, triaxial operation for a single ^{87}Rb cell tends to sacrifice sensitivity as a laser beam splitter is required for this architecture (Boto et al., 2022), which halves the power, and increases noise floor; and adding closed-loop operation increases the complexity of the support electronics. Even if such a sensor were practical, MEG measurements would still be contaminated by artifacts induced by translation and rotation of a magnetometer in the non-zero MSR field. Movement artifacts can be reduced significantly by synthesizing gradiometric response using an array of reference sensors (Vrba and Robinson, 2002). The FieldLine (Boulder, CO USA) OPM sensors support closed-loop measurement on a single sensing axis but are configured for static nulling of the transverse fields. These sensors are thus susceptible to nonlinearity due to CAPE and motion artifacts. Since the FieldLine support electronics can provide user control of the field coil offsets, we have developed dynamic field compensation (DFC) as a solution to CAPE. When applied in tandem with synthetic gradiometry and closed-loop operation, DFC is capable of dramatically attenuating errors due to both CAPE and movement artifacts.

DFC, as proposed in this work, obtains the ambient vector magnetic field measurement from an orthogonal array of OPM reference magnetometers. Closed-loop mode is used on all OPMs to maintain null on the sensing (b_Z) axis. The time-varying reference field measurements are used to dynamically update the current delivered to the OPM transverse nulling coils (b_X and b_Y) on all sensors, thereby compensating for dynamic field offsets on all three axes. Thus, under the assumption of operation within a uniform time-varying field, the primary and reference sensor gains will not be perturbed by magnetic field fluctuations, within their dynamic range. Furthermore, the reference field values computed for each primary sensor b_Z axis can be subtracted from its measurements, giving it a 1st-order gradient response. The primary sensors, thus configured as synthetic gradiometers, will not respond to translation and rotation. We demonstrate that, using DFC, an OPM array can obtain robust, precision measurements (less than 1% gain error) in the presence of 1-5 nT perturbations in the ambient transverse field. In addition, we show that DFC, combined with synthetic gradiometry, can markedly attenuate artifacts due to head movement in a uniform field.

2. Materials and Methods

2.1. OPM Instrumentation

Each FieldLine (Boulder, CO) v2 OPM sensor is comprised of a 3 × 3 mm^3 cell containing ^{87}Rb vapor, a heater, laser diode, photodiode, optical components, and three internal orthogonal field coils within a 13 × 15 × 30 mm^3 housing. A shielded ribbon cable connects each sensor to the multichannel control electronics. The cable provides power for the laser, photodiode, and heater, signals from the photodiode and field nulling coils, plus modulation and feedback signals. The cable connector to the OPM control electronics contains an EPROM (erasable programmable read-only memory) with embedded tuning parameters for plug-and-play operation. FieldLine's sensor design reduces heat exposure of the laser to the hot vapor cell ensuring that the laser can be reliably stabilized to the atomic transition. In addition, the OPM controller incorporates algorithms for rapid and reliable ambient field nulling in non-ideal magnetic environments in MSRs with high offset fields and large power line frequency interference. Each sensor can be operated in closed-loop mode on its sensing z-axis using a self-shielded double Helmholtz coil designed to reduce crosstalk (Nardelli et al., 2019). The sensor axes are established by the laser path and modulation coils (Figure 1A). These axes are labelled b_X, b_Y, and b_Z, with modulation applied to b_Z making it the sensing axis; b_X and b_Y are the transverse axes (Figure 1B). The x and y-axis field coils are higher-order Helmholtz-like designs and are used for statically nulling the transverse field. The multichannel OPM control electronics chassis accommodates up to 16 sensors and one A/D (analog-to-digital) channel. Multiple chassis can be daisy-chained and synchronized to accommodate up to 512 sensors. All functions, includ-

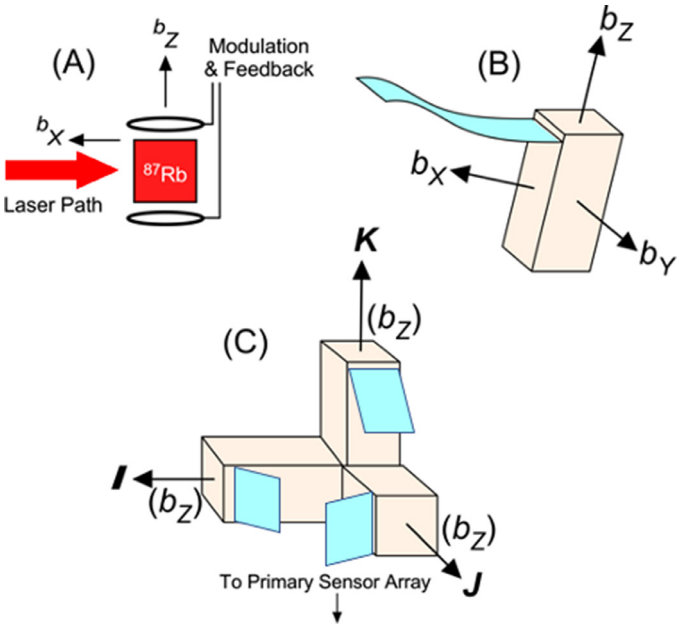

Figure 1. OPM sensor and array axis definitions: (A) Two of the sensor vectors are determined by the path of the laser beam through the rubidium vapor cell (b_X) and the orientation of the modulation coils (b_Z), The third vector, b_Y,is orthogonal to these forming a right-handed coordinate system The transverse axes, (b_X) and (b_Y) also have pairs of coils (not shown) for nulling the field. The rubidium cell is offset 5 mm from the base of the sensor housing. (B) The independent coordinate system of each sensor is indicated relative to the ribbon cable orientation, with positive b_X directed toward the cable. (C) The orientation of the 3D-printed sensor fixture is defined by the vectors I, J, and K of the reference OPM array. These axes are aligned with each reference OPM sensing vector (b_Z).

ing data acquisition, modulation, detection, field nulling, and closed-loop feedback are controlled internally by an FPGA (field-programmable gate array) and onboard host CPU (central processing unit). An Ethernet cable provides communication for data and commands between the controller and a Linux or PC workstation. Control functions are commanded using a set of Python APIs. FieldLine OPM sensors have a nominal sensitivity ~15 fT/$\sqrt{\text{Hz}}$ and may be operated in either open-loop or closed-loop mode. In open-loop mode the sensor response is -3dB at 150 Hz. The closed-loop bandwidth, selected by FieldLine, represents a trade-off with sensitivity. In practice, the bandwidth is established by adapting the coefficients of a closed-loop proportional integral device (PID) controller to flatten the frequency response. These coefficients are computed adaptively once and are stored for each individual sensor. In closed-loop mode both amplitude and phase response are equal for all sensors. The sensor operating range is ±100 nT, with a closed-loop dynamic range of ±15 nT. The standoff of the FieldLine sensor is 5 mm, meaning that the center of the ^{87}Rb cell is offset 5 mm from the base of the sensor housing.

The D/A (digital-to-analog) converters on the FieldLine controller supply the currents applied to the three orthogonal field coils of each OPM. In normal operation, the controller applies static currents to null the field for each axis using a zeroing algorithm executed before the start of data acquisition. In open-loop mode, all three nulling coil currents remain fixed throughout operation. In closed-loop mode, the controller applies a time-varying current to the sensing axis (b_Z) to dynamically maintain null field, making the measurement proportional to the applied feedback current, while the transverse axis nulling coils remain static. This leaves the OPM sensor susceptible to CAPE errors due to ambient transverse fluctuating fields. While time-varying modifications to the transverse axis nulling coils are not currently implemented as standard operation of FieldLine sensors, the sensor controller architecture uniquely permits dynamic control of the transverse (b_X and b_Y) field coils, enabling the implementation of DFC for mitigation of CAPE.

2.2. Sensor Configuration for Cross-Axis Dynamic Field Compensation

Consider an OPM system configured as a fixed array of three orthogonal reference OPM sensors and multiple primary OPM sensors. To understand the operation of the DFC we first define the coordinate system. The sensor fixture axes, labeled *I, J*, and *K* (to avoid ambiguity with the OPM sensor axes) are defined by the vectors representing the sensitive directions of the three orthogonal reference magnetometers (Figure 1C); the orientation of the references defines the coordinate system for the array. We refer to each reference sensor by the axis it defines – e.g., the *K* reference defines the *K* axis of the array. Each OPM sensor operating in closed-loop mode measures the field along its z-axis (b_Z). The orientation vectors of each primary sensor nulling coil are determined relative to the reference magnetometer axes and are independent of the orientation of the array within MSR.

2.3. DFC Mathematical Derivation

As introduced earlier, the objective of DFC is to reduce the transverse fields within the OPM cell so that CAPE is minimized. Assuming that the ambient fields responsible for CAPE are uniform, we can derive appropriate fields to apply to the coils from a triaxial reference array. Consider that the three reference magnetometers measure, along their b_Z directions, the ambient fields in the *I, J*, and *K* directions; these fields are denoted $B_I(t)$, $B_J(t)$, and $B_K(t)$, respectively, where t denotes time or sample. Assuming that these fields are uniform, the compensation field at the x, y, and z-field coils for any arbitrarily oriented coil can be derived by multiplying the reference field vector $\boldsymbol{B}(t)$ by a rotation matrix $\boldsymbol{\alpha}$ that represents the transformation from the orientation of the primary sensor to the orientation of each reference sensor.

$$\begin{bmatrix} b_x(t) \\ b_y(t) \\ b_z(t) \end{bmatrix} = \begin{bmatrix} -1 \\ -1 \\ -1 \end{bmatrix} \begin{bmatrix} \alpha_{xI} & \alpha_{xJ} & \alpha_{xK} \\ \alpha_{yI} & \alpha_{yJ} & \alpha_{yK} \\ \alpha_{zI} & \alpha_{zJ} & \alpha_{zK} \end{bmatrix} \begin{bmatrix} B_I(t) \\ B_J(t) \\ B_K(t) \end{bmatrix} \tag{1}$$

In practice, because field null is maintained by closed-loop operation on the z-axis for each sensor, the b_Z component is not applied to the nulling coil. Instead, we can use the b_Z component to synthesize 1st-gradient response. This is accomplished in software by subtraction of the transformed references from each primary sensor: $\dot{B}_Z(t) = B_Z(t) - \alpha_Z \cdot B_{refs}$. Note that the 1st-gradient baseline differs among sensors because their distances from the reference array varies. Due to the lack of a fixed baseline, our synthetic gradiometer measurements will be expressed in units of Tesla instead of T/m. This convention has also been used for synthetic gradiometer measurements from a SQUID-based MEG instruments (CTF Systems, Inc.).

Compensation of the three reference sensors is simplified because they are oriented at right angles to one another; with the rotation matrices for the *I, J,* and *K*-axis references OPMs, based on their orientations in the sensor fixture, is given by:

$$\begin{bmatrix} 0 & 1 & 0 \\ 0 & 0 & 1 \\ 0 & 0 & 0 \end{bmatrix}, \begin{bmatrix} 1 & 0 & 0 \\ 0 & 0 & -1 \\ 0 & 0 & 0 \end{bmatrix}, \text{ and } \begin{bmatrix} 0 & 1 & 0 \\ -1 & 0 & 0 \\ 0 & 0 & 0 \end{bmatrix}, \text{ respectively.} \tag{2}$$

Thus, the reference sensor transverse axes are compensated as follows:

$$\begin{array}{lll} b_x^{\mathrm{I}}(t) = -B_{\mathrm{J}}(t) & b_x^{\mathrm{J}}(t) = -B_{\mathrm{I}}(t) & b_x^{\mathrm{K}}(t) = -B_{\mathrm{J}}(t) \\ b_y^{\mathrm{I}}(t) = -B_{\mathrm{K}}(t) & b_y^{\mathrm{J}}(t) = B_{\mathrm{K}}(t) & b_y^{\mathrm{K}}(t) = B_{\mathrm{I}}(t) \end{array} \tag{3}$$

This arrangement dynamically maintains zero field for all reference-magnetometer axes, assuming that static offsets in the ambient field have been correctly nulled before the DFC compensation is applied. Note here that the compensation-field current is added to the previously determined static nulling current. This dynamic compensation on

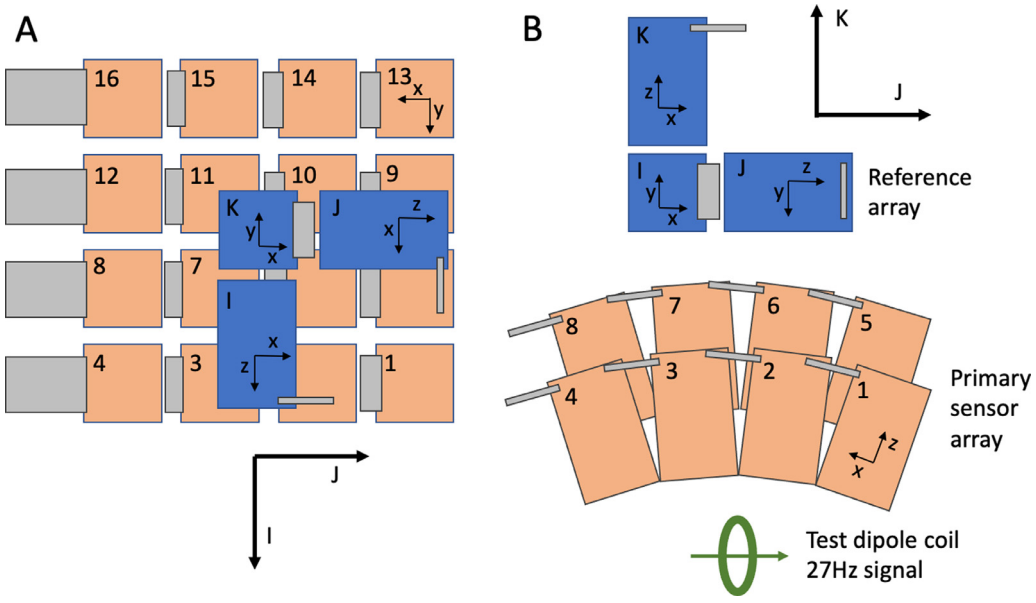

Figure 2. The orientation of the sensor fixture and reference array shown from (A) above and (B) the side. Reference sensors are shown in blue, and primary sensors in peach. A portion of the ribbon cable from each sensor is shown in grey. The coordinate system of the array is defined by the bz vectors of the I, J, and K reference OPM sensors, as indicated by the large black axes. Each OPM sensor has an independent coordinate system defined as in Figure 1, as shown by the small black axes indicated on some individual sensors. Also shown in (B) is the test dipole coil.

the transverse axes mitigates measurement error due to CAPE if the ambient fields, and any fluctuations in the ambient fields, are uniform, with no gradients. The concurrent use of closed-loop operation, DFC, and synthetic gradiometry mitigates inherent nonlinearity, eliminates CAPE effects, and reduces artifacts when the fixed array is rotated in a uniform background field or translated in the presence of field gradients (Vrba and Robinson, 2002).

2.4. Experimental Setup

To test the performance of the DFC procedure, we used 19 OPMs and two FieldLine controller chassis. Sixteen OPMs (controlled by one chassis) were inserted into a rigid 3D-printed 4 × 4 sensor fixture which contained slots for each sensor to precisely fix the orientation (Figure 2). Three additional OPM sensors (controlled by another chassis) were used as reference magnetometers for the *I, J*, and *K*-axes and were mounted orthogonally in a fixture approximately 5 cm above the primary array. One primary sensor was not operational, and DFC was not correctly applied to another primary sensor during some of the experiments. The orientation vectors for the b_x, b_y, and b_z -field coils of each OPM were computed from measurements in the 3D-printed fixture design file. All experiments were carried out in a magnetically shielded room (MSR) having two mu-metal layers and one aluminum eddy current shield (model Ak3b, Vacuumschmeltze GmbH & Co. KG, Hanau, Germany). A bi-planar set of MuCoils (Magnetic Shields Ltd, Kent, UK) was set up in the MSR to provide additional reduction in ambient fields and gradients around the sensors. Initial calibration of the MuCoils is achieved using measurements from two tri-axial fluxgate magnetometers which are removed from the MSR prior to starting OPM experiments. All data, comprised of the primary and reference OPM field measurements and derived channels for filtered references, compensation fields, and first gradients, were collected at a 1 kHz sample rate. Python scripts using the FieldLine APIs (available for download at https://github.com/nih-megcore/OPMLab) were used for data acquisition and dynamic control of the currents on the transverse axes. A known signal is required to measure CAPE-induced errors in gain. A magnetic dipole test coil (CTF, Coquitlam, BC, Canada) positioned beneath the sensor array (shown in Figures 2 and 3) was energized by a sine wave supplied by in-house custom calibration electronics comprised

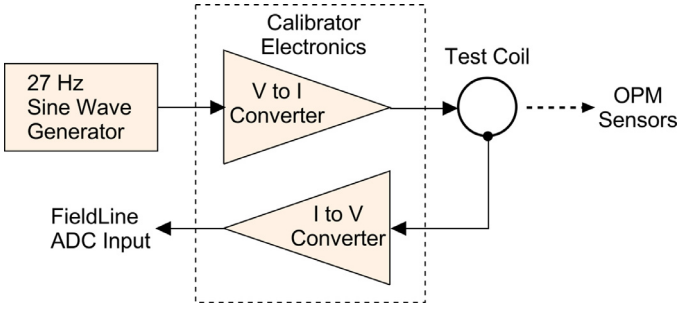

Figure 3. OPM test diagram. A function generator producing a 27 Hz sine wave is connected to custom built calibrator electronics located outside the MSR. A voltage-to-current stage drives one of 36 test dipole coils located inside the MSR. A current-to-voltage converter monitors the coil current. The array of OPM sensors detects the AC field of the test dipole coil. A voltage, proportional to coil current, is monitored by one of the FieldLine ADC channels.

of a function generator, a current driver, and a current monitoring output (Figure 3). This coil, along with 35 others, was supported in a rigid 3D-printed hemispheric dome constructed for calibration of our OPM sensor array; only one coil was used in the described experiments. The calibrator coil was energized by applying a 2.0-volt peak-to-peak (p-p) 27-Hz sine wave input to the calibrator electronics using a function generator; this corresponded to a current of 1.0 mA p-p, yielding a magnetic moment of 2.0583 $\times 10^{-7}$ A-m^2 p-p. The calibration frequency of 27 Hz was selected by finding a region in the spectrum where sensor noise was low and free of environmental interference. The test coil was located approximately 70 mm below the center of the reference array and 20 mm from the primary sensors. This yielded an AC field ranging from 37 to 108 pT rms measured by the primary sensors. Output of a current monitor was recorded during acquisition using the A/D input on the FieldLine controller.

2.5. DFC Procedure

Data acquisition using DFC proceeds as follows. First, all OPM sensors are statically nulled along all three axes and closed-loop operation

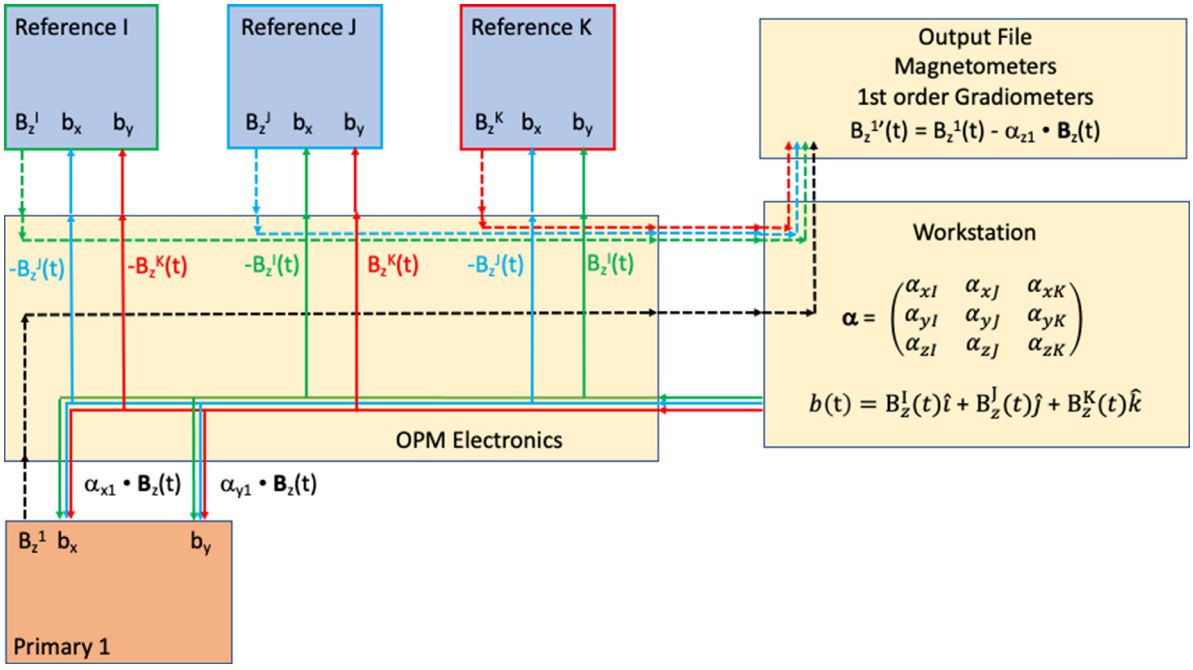

Figure 4. Cross-axis dynamic field compensation computation. Only four OPM sensors (all three references and one primary sensor) are shown to illustrate the data flow between the OPM electronics and a Linux workstation. The closed-loop field values for all sensors (B_Z, denoted by dashed lines) are sent to the workstation via ethernet. The dynamic compensation fields, b(t), are computed within the workstation using the rotation matrices for each sensor and sent to the controller. The compensation is applied to the transverse coils of both the references and the primary sensors by the D/A converters within the controller. The calibration field currents are added to the previously determined static nulling currents. Note that compensation of the references is simplified due to the orthogonal orientation. In addition, 1st-gradient response is synthesized within the workstation by subtracting the compensation for the b_z vector for each primary sensor.

is initiated on the sensing axis. DFC is then implemented on the reference sensors and the primary sensors simultaneously. The B_Z fields from the three (*I, J,* and *K*) reference sensors are lowpass filtered by a one-pole, exponential-decay IIR lowpass filter. The moving average $\bar{B}_t$ is updated as each new sample B_t is acquired. This relatively simple and computationally efficient filter serves to reduce the 60 Hz power-main interference while leaving the slower low-frequency ambient-field fluctuations unchanged. The filter updates the moving average $\bar{B}$ with each new measured sample B, in real-time, according to:

$$\bar{B}_t = kB_t + (1-k)\bar{B}_{t-1}, \tag{4}$$

where $k = e^{-1/\tau F_s}$. For $\tau = 0.01$ s and a sample rate $F_S = 1000$ Hz (giving k=0.905), the -3dB cutoff frequency is 8.4 Hz. The instantaneous DFC compensation is calculated as in Equations 1-3 and then applied to the transverse coils (b_x and b_y). This process is illustrated in Figure 4. The delay between sensor static nulling and the start of acquisition was approximately 10 ms – assuring that there are no significant sensor field offsets prior to starting DFC. Minimizing the time between static nulling and starting DFC is important because DFC cannot correct for CAPE if there are significant uncorrected initial static offsets.

2.6. Validation Experiments

Validation experiments were performed to determine the CAPE-induced errors in effective gain, both with and without DFC under stationary conditions and during movement. As described in Section 2.5, each acquisition began by statically nulling all OPMs, initiating data acquisition with or without DFC, followed by energizing the 27 Hz test magnetic dipole. For the initial DFC validation tests, data were recorded for 300 seconds both with DFC off and with DFC on. An additional recording was acquired where DFC was applied to only some of the primary sensors, and experiments were repeated with and without the MuCoils active. For these validation recordings, our laboratory main door (not to be confused with the MSR door) was opened at approximately 100 s and 200 s to induce additional fluctuations in the ambient field. A second set of experiments was carried out to demonstrate the effects of motion of the array in the residual field. The entire assembly, including the test-coil assembly and the array fixture, was placed on a turntable, and manually rotated during the acquisition by an experimenter in the room during a 90 s recording. Excursions of up to ±20 degrees were used, and experiments were repeated with and without the MuCoils activated. We expected that MuCoils would be required to obtain adequate control of CAPE when array movement is present. For the motion tests, we present the field measurement from the magnetometers, as well as the synthetic gradiometers, calculated according to the derivation in Section 2.3.

2.7. Data Analysis

To determine the rms power of the measured 27-Hz signal in each run, a Hanning-windowed FFT was applied to 2-s segments (with 50% overlap) of data from each sensor. The percent change in the measured rms test signal was computed relative to its magnitude when the absolute value of the total reference field was closest to zero. We use this value as a proxy for the true field, given that the rms signal should be closest to its true value when the ambient-field offset is smallest, and refer to this value as B_0. For visualization, we calculate the time series of the ambient field (B_z from the *I, J,* and *K* reference sensors) using the average of overlapping 2-s segments. In addition to plots of the time series, we also show scatter plots of the magnitude of the ambient field versus the measured magnitude of the 27-Hz rms power for each 2-s window. To best show the effects of each component of the magnetic field, the reference fields from the *I, J,* and *K* magnetometers are transformed to the internal x, y, and z axes of the sensor, using the rotation matrices ($\boldsymbol{\alpha}_n$) derived for the DFC procedure. To illustrate the effects (if any) of DFC on the sensor noise floor, we present averaged spectra, with and without DFC, computed for overlapping 4-s time segments (0.25 Hz resolution). For our tests incorporating motion of the sensor array, we also

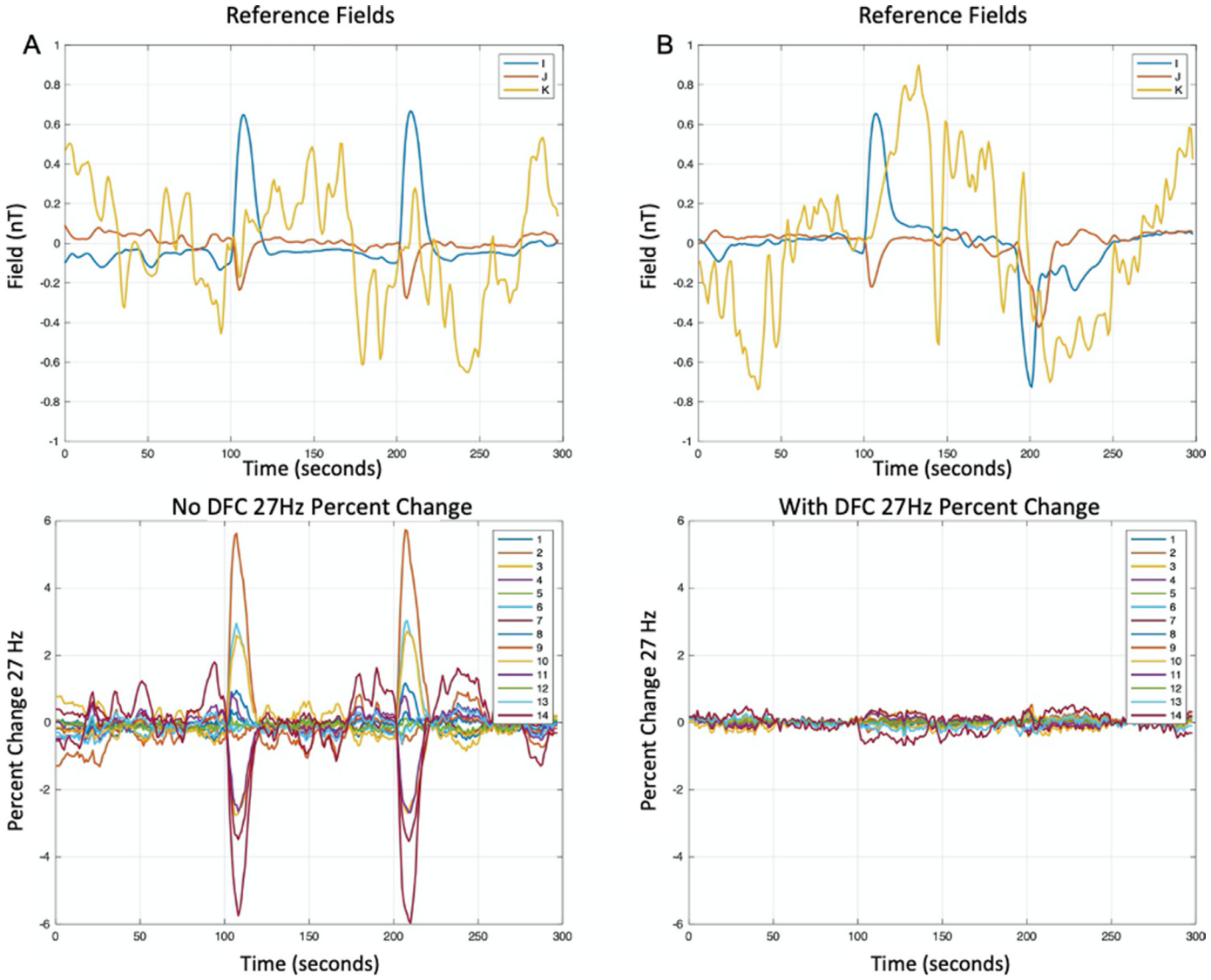

Figure 5. Percent change (effective gain error) of the 27-Hz calibrator signal induced by fluctuation in the ambient field. The laboratory door was opened and closed around 100 s and 200 s.(A) Without DFC there are large changes in effective gain. (B) With DFC, the induced changes in effective gain are reduced. Note that sensor 14 was not operational and DFC was not correctly applied to sensor 16. Note that, although there are significant fluctuations in the ambient field in the K-direction, the measured primary sensor 27-Hz signal magnitudes are relatively insensitive to those changes, because their sensing axes (b_Z) are also oriented mostly in the K-direction. The largest gain errors are due to the I-direction ambient field fluctuations. This corresponds to the primary sensors b_Y axes that are perpendicular to the direction of the laser beam (see Figure 2 for correspondence of reference and primary sensor axes).

calculate and plot the average field measured by each sensor, calculated using the average over 2-s time windows.

3. Results

Figure 5 illustrates a comparison of 14 primary sensors in two separate acquisitions, one with and one without DFC (one primary sensor was not operational and DFC was not correctly applied to another). Ambient fluctuations reached approximately 704 pT and 904 pT when the laboratory door was opened for the uncompensated and compensated datasets, respectively. In the uncompensated acquisition, we observed significant modulation of the 27 Hz test signal, with a maximum effective gain change of 5.96 percent when the laboratory door was opened and a mean ± standard deviation of 2.05 ± 1.93 percent (Figure 5A). Cross axis DFC significantly reduced the modulation (effective gain change) induced by ambient field fluctuation via CAPE, with a maximum change of 0.68 percent and mean ± standard deviation of 0.33 ± 0.16 percent (Figure 5B). Note that while some sensors are profoundly affected by CAPE, others show far less variation with the ambient field. These variations may be partially explained by initial reference field offsets and errors in sensor geometries. Variations in the ambient field measured by the *I*-magnetometer appear to have the greatest effect on gain errors.

An additional dataset was collected for which only some OPM sensors had dynamic field compensation. The peak ambient field fluctuation was 819 pT (Figure 6A). The 8 OPM sensors without DFC had a maximum effective gain change of 5.18 percent and mean of 2.05 ± 1.55 percent (Figure 6B). The 7 OPM sensors with DFC had a maximum change of 0.33 percent and a mean of 0.27 ± 0.04 percent (Figure 6C).

The relationship of the field measured by each primary sensor to the offset of the ambient field from null can be represented as a scattergram. Figure 7 shows the scattergrams of the measured 27 Hz rms magnitude versus the I, J, and K reference ambient field components transformed to the internal orthogonal sensor axes for a typical primary sensor (channel 13) using Equation 1. While the sensor dependence on ambient fluctua-

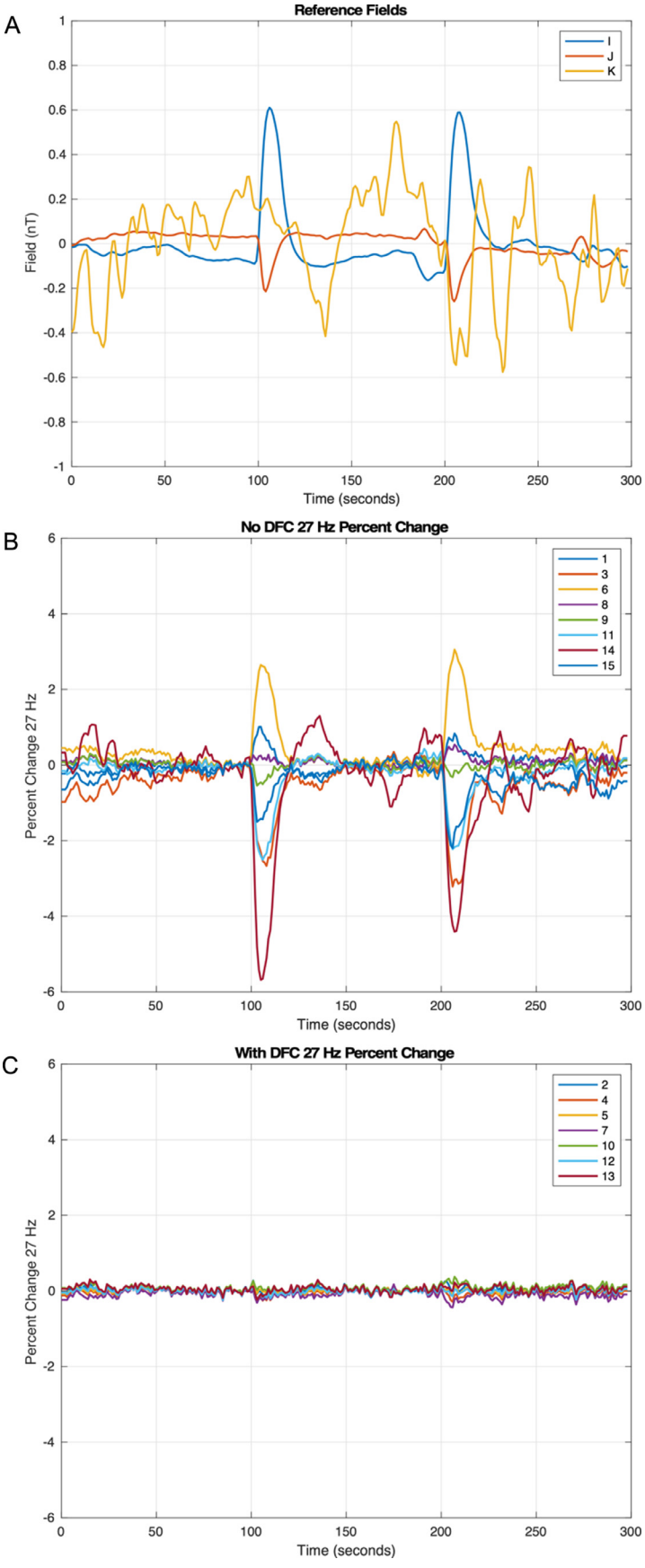

Figure 6. Percent change (effective gain error) of 27 Hz test signal versus ambient field fluctuations. The laboratory door was opened and closed around 100s and 200 s. (A) Ambient field fluctuations measured by reference sensors; (B) effect of ambient field on OPM measurements of the 27Hz test signal without DFC; (C) effect of ambient field on OPM measurements of the 27Hz test signal with DFC. Note that sensor 14 was not operational.

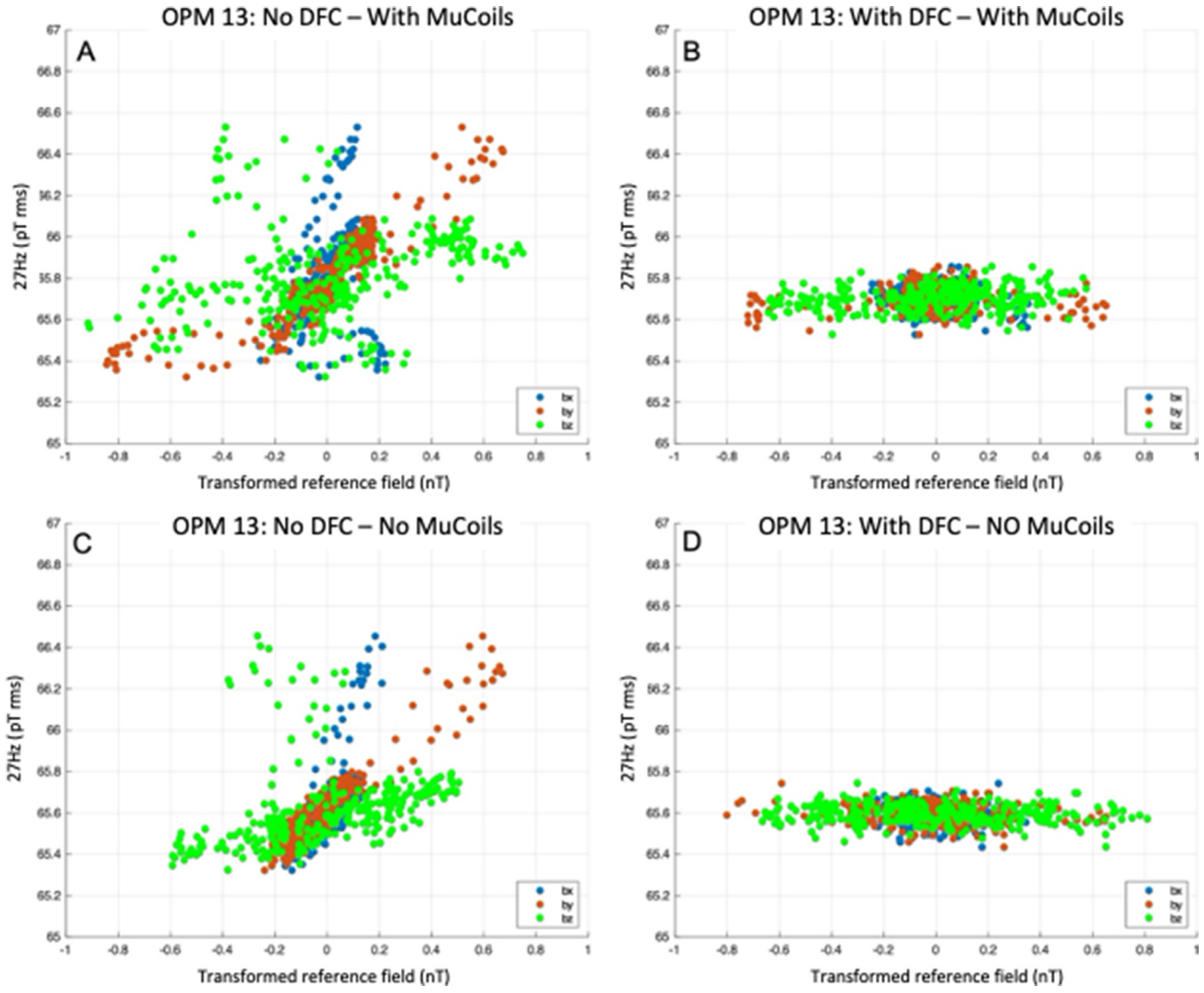

Figure 7. Scatterplots illustrating the power of the 27-Hz test signal plotted versus the fluctuations in the ambient field transformed to the b_X, b_Y, and b_Z sensor coordinate frame (illustrated in Figure 1) for a single primary sensor (sensor 13), using Equation 1. Panels A and C illustrate the no DFC condition, while panels B and D illustrate the condition with DFC applied. Note that in Panels B and D, the compensation fields are equivalent to the transformed reference fields. Panels A and B illustrate a recording acquired with MuCoils on, while C and D illustrate a recording with MuCoils off. Note that because the OPM nulling coils zero the field in the cell at the beginning of the measurement, the fluctuations in the ambient field are comparable with and without the static MuCoils active.

Table 1
Linear Regression slopes for the measured 27 Hz rms field versus transformed reference compensation fields averaged across all 15 primary sensors. Statistics values are for the absolute value of the slopes. Values shown are the mean ± standard deviation with units of pT(rms)/nT. The apparent differences between DFC with and without MuCoils is likely a consequence of differences in ambient field fluctuations at the time of measurement.

	No DFC No MuCoils		No DFC With MuCoils		DFC No MuCoils		DFC With MuCoils	
	Mean	Std Dev	Mean	Std Dev	Mean	Std Dev	Mean	Std Dev
b_X	1.5684	1.1927	0.8585	0.6811	0.0304	0.0183	0.1244	0.0625
b_Y	0.9529	0.1403	0.6335	0.1200	0.0415	0.0061	0.0093	0.0060
b_Z	0.3242	0.0779	0.2649	0.0778	0.0144	0.0013	0.0343	0.0042

tions contains nonlinear terms, we can nonetheless obtain a rough linear fit of the sensor response versus the ambient field. The mean and standard deviations of the absolute values of the slopes for a linear fit of the primary OPM signals versus the transformed reference fields for the x, y, and z-axis of each primary sensors is summarized in Table 1. Without DFC the regression slopes are large – indicating a dependence of the sensor "effective gain" on the field deviations from null (Figures 7A and 7C). With DFC enabled, the slopes are much smaller – showing that effective gain is independent of the field deviations (Figures 7B and 7D). Note that the variation in the slopes across sensors is likely due to issues with the accuracy of the initial nulling of each sensor cell or imperfections in the internal sensor geometry.

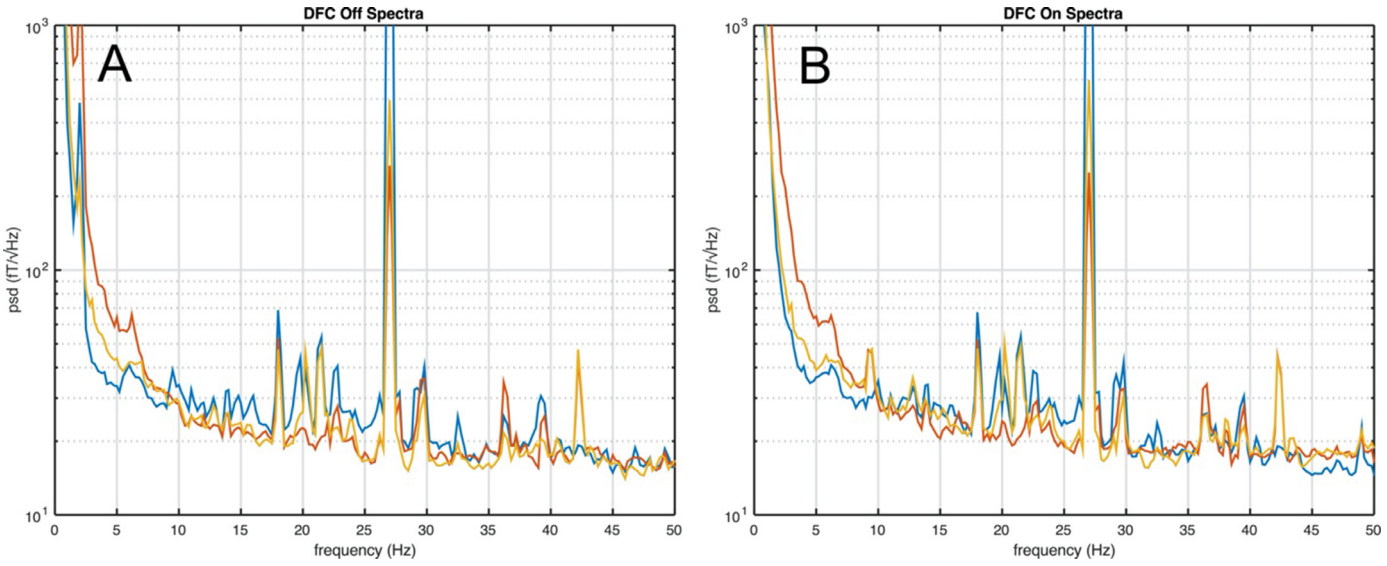

Figure 8. OPM averaged (truncated) spectra, with and without DFC (MuCoils on). Three representative OPM sensors are shown. Average of 149 4.0-second time segments with 50% overlap. Panel A shows spectra without DFC compensation off Panel B shows spectra with DFC compensation on. DFC does not attenuate environmental magnetic noise. Instead, DFC mitigates changes in effective sensor gain due to CAPE. With DFC off, the averaged spectra include fluctuations in effective gain. Aside from CAPE and differences in ambient magnetic noise, the spectra are nearly identical.

The effects of DFC on sensor noise were evaluated by computing the averaged power spectral density for the two 180-second recordings shown in Figure 8. Spectra were computed for 149 4-second Hanning-windowed segments, with 50% overlap. The peak-to-peak ambient field fluctuations were 704 pT and 904 pT for the DFC off and DFC on datasets, respectively. These results demonstrate that DFC does not significantly increase sensor noise. The small spectral differences between DFC off and on are attributable to differences in ambient field fluctuations.

Finally, we show the relative contributions of DFC and 1st-order gradiometry on the measured signal when motion (specifically rotation) of the array is present. In Figure 9 A, B, C, D, and E, we show results with DFC active, and in Figure 9 F, G, H, I, and J we show results without DFC. When 1st-order gradiometry is used without DFC, errors in the gain of sensors, measured as perturbations in the measured 27-Hz field power, are still evident (Figure 9H), as expected, although overall low-frequency fluctuations in the signal amplitude are suppressed (Figure 9J). In contrast, DFC is capable of sharply attenuating errors in sensor gain, even in the presence of motion (Figure 9B), provided that ambient fields are attenuated using the MuCoils. The MuCoils are required because motion of the sensors within the MSR static field of 30-40 nT can exceed the ±15 nT dynamic range of the OPMs operating in closed-loop mode. The combination of DFC and 1st-order gradiometry has the effect of both reducing CAPE errors and low-frequency motion artifacts (Figure 9C and 9E).

4. Discussion

In this manuscript, we demonstrate that DFC is effective at eliminating gain errors due to transverse field offsets (CAPE) for ambient-field fluctuations in the range of ±1 nT. Under conditions with no movement, CAPE can induce errors up to 5% in our typical MSR environment, which are reduced to < 0.7% when DFC is applied (See Figures 5 and 6). Furthermore, the combination of DFC and 1st-order gradiometry reduces both motion-induced artifacts and gain errors in sensor response. Although DFC is sufficient to suppress CAPE effects due to ambient field changes in our ak3b MSR, it may not be adequate for compensating field excursions exceeding the closed-loop dynamic range of ±15 nT, as occurring during large subject movements. In such cases, external field compensation methods such as biplanar nulling coils are required (as demonstrated in Figure 9).

The effects of CAPE have been previously reported in the literature (Boto et al., 2017; Iivanainen et al., 2019). The theoretical basis of CAPE was extensively explored in Borna, et al. (Borna et al., 2021). In an ideal setting, the polarization of the vapor along the laser propagation axis (the x-axis in the FieldLine sensor) encodes information only about the magnetic field along the sensing axis (z) at the modulation frequency, taking the form of a dispersion curve. Borna, et al. (Borna et al., 2021) describes the impact of residual fields along the laser propagation axis, using both simulations and experiments. While the derivation of CAPE errors presented in Borna, et al. (Borna et al., 2021) includes both transverse field axes, Borna explicitly makes the assumption that $b_Y \ll b_X$ (in the FieldLine version 2 sensor coordinate system) to derive a simplified set of differential equations. Our results demonstrate that in a typical laboratory environment, the transverse fields perpendicular to the laser propagation axis cannot be neglected, and will have a significant impact on the OPM sensor response. Transverse fields perpendicular to the laser axis have the effect of perturbing the angle of the sensing axis to a significant degree, which result in artificially increased or decreased measured signal, depending on the topography of the signal of interest. Our results show that without DFC the effect of the ambient field on CAPE varies among sensors. This can in part be attributed to differences in orientation of each sensor relative to the ambient vector field and to the accuracy of the static field nulling on the sensor transverse axes.

There are several technical considerations that merit further discussion. First, this DFC implementation compensates only for changes in the uniform (zero-order) field and does not account for gradients. However, with additional reference sensors beyond the three orthogonal sensors used in this study, CAPE due to both uniform fields and gradients can be eliminated, and higher order gradiometer response can be synthesized to improve signal to noise, particularly when head movement is present (Vrba et al., 1998; Vrba and Robinson, 2001). In our prototype array, the triaxial reference array had a nominal baseline of approximately 5 cm to the primary sensors. Minimizing the baseline serves to reduce the effect of gradients on the field compensation. However, the baseline must be large enough that brain signals are not significantly attenuated by synthetic gradiometry. When synthesizing 1st-order gradiometer response for rejection of magnetic interference, it has been shown that shorter

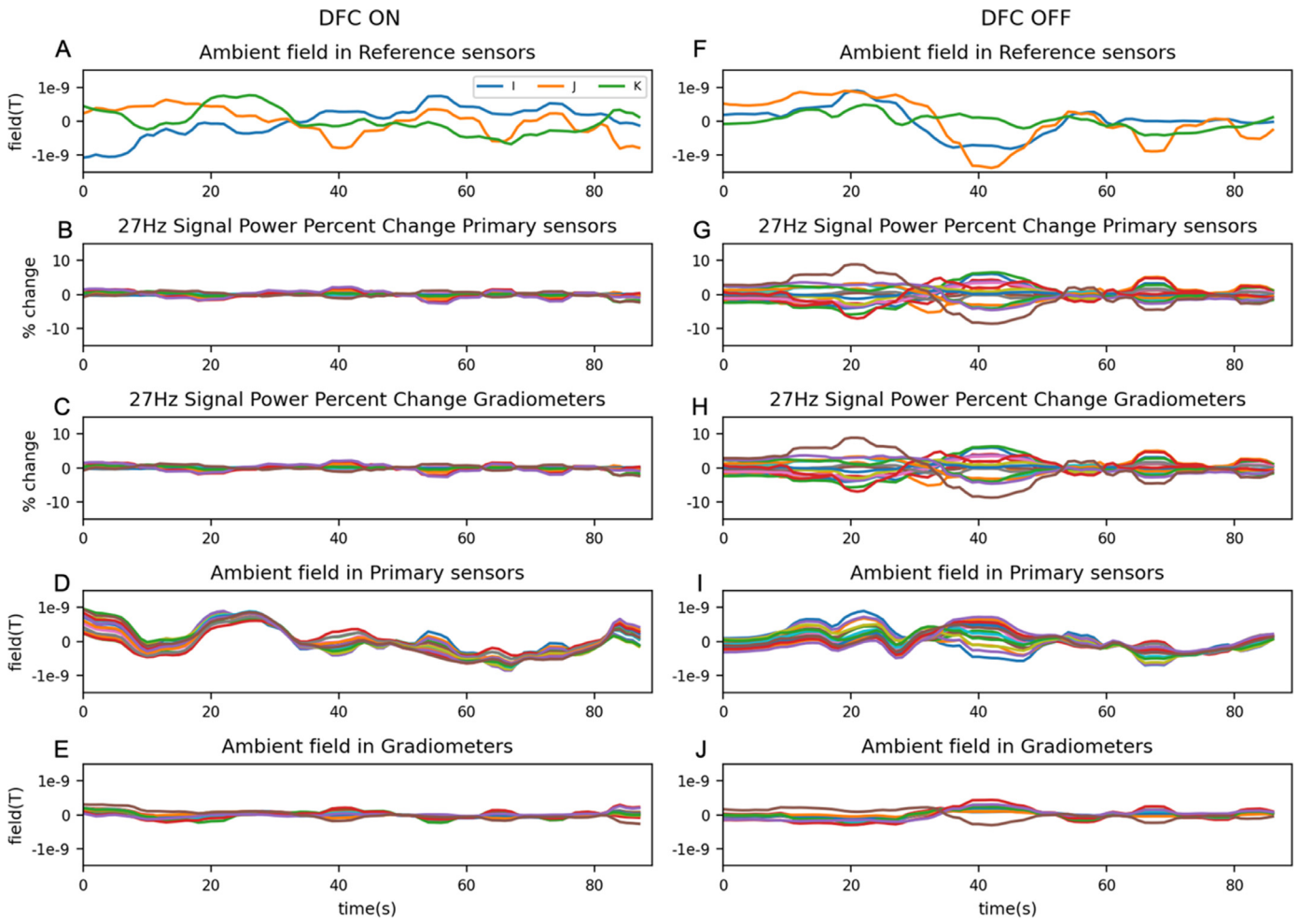

Figure 9. Dependance of the measured 27-Hz signal magnitude to the reference ambient fields during rotation. Panels A and F show the ambient field as measured by the reference sensors. Panels B and C show the magnitude of the 27Hz reference signal as measured by OPM magnetometers and synthetic gradiometers, respectively, with DFC on. Panels G and H show the same, but without DFC. Without DFC, the effects of motion on the gain are clearly visible. Panels D and E show the fluctuations in the background field measured by the primary magnetometers and synthetic gradiometers, respectively, obtained by a moving average over 2s windows (with 50% overlap). Panels I and J show the same but without DFC. It is evident that neither DFC nor synthetic gradiometry alone can attenuate errors resulting from motion in a background field, yet the two together can reduce the impact of both CAPE gain errors and motion artifacts (Panels C and E).

baselines of 2-5 cm are most effective and do not significantly reduce sensitivity to deeper MEG sources (Vrba and Robinson, 2002).

A hardware triaxial reference array was required for our demonstration of DFC. An alternative approach would be to derive all three reference components from the primary sensors array measurements using a low-order spherical harmonic expansion (Tierney et al., 2021). However, since the primary sensors of our array are nearly parallel to the *K*-axis, the remaining references axes would be poorly determined (see Figure 2); thus, this method is most appropriate for large sensor arrays having whole-head coverage, such that the entire vector ambient field is sampled. Derivation of the uniform field from the sensor array implies a loss of three degrees of freedom and potentially reduced accuracy compared to a hardware reference array. In addition, when using the primary sensor array to derive the reference fields, the measured fields must be lowpass filtered to attenuate the influence of the MEG signals. This filtering limits the ability of DFC to compensate for rapid changes in ambient field and head movement. Because of this frequency limitation we recommend employing a separate physical reference array for best DFC performance. More complex reference arrays may also be utilized to provide redundancy (in the worst case) and higher order gradiometry (in the best case). The DFC technique crucially relies upon uninterrupted operation of the reference sensors, and thus requires a high degree of reliability. While only one (primary) sensor failure during this study, spare sensors are recommended for DFC MEG measurements.

Our test configuration employed a 27 Hz magnetic test signal for the purpose of evaluating CAPE-induced gain changes. We introduced a reference lowpass filter (with a -3dB cutoff of approximately 8.7Hz) to attenuate the peak-to-peak test signal so that it was smaller than the transverse axes D/A converters resolution of 4.6 and 3.0 pT per step for the b_X and b_Y axes, respectively. This filter was sufficient to allow compensation of the slower changes in ambient magnetic interference as is evident from the reduction in effective gain changes. Since DFC was implemented in software on the host workstation, there is a 1 ms delay between acquiring the reference field measurement and application of transverse axis compensation by the FieldLine electronics. This introduces a phase delay error that is proportional to frequency that would degrade compensation for large and high frequency signals such as the 60 Hz power frequency and its harmonics, further necessitating the use of a reference lowpass filter. Another consideration is the potential for DFC to couple noise into the primary sensors. Crosstalk between the sensor transverse axis field coils and the sensing axis could potentially introduce noise, depending on the magnitude of crosstalk; reference sensor noise could also potentially affect primary sensor noise. Based upon the sensor spectra with and without DFC (Figure 8), both effects appear

to be small. Reference sensor noise is vectorially additive to the noise level of synthetic 1st-order gradiometers.

There are several important limitations to note. First, the application of DFC depends crucially on the physical structure of the entire sensor array. Here we used a rigid 3D-printed fixed array of OPMs, where the orientations of all sensors are precisely known. Any fitted array, where sensors are inserted in openings and adjusted radially to be in close contact with the scalp, may be readily used with DFC because only the field coil orientation vectors and not their locations are required. Flexible EEG-type cap designs are not appropriate for use with DFC. Additionally, accurate transverse-axis field compensation depends upon the precision of the initial static field offsets of all three axes of the primary and reference OPMs. Dynamic compensation derived from the references is additive to the existing transverse field static offsets. Small offset errors in transverse fields are likely to be random, but transverse-axis field compensation depends upon the accuracy of the three reference OPMs. As such, the initial reference measured fields should be as small as possible after nulling.

Given the finite field resolution of the D/A converters delivering the nulling currents, DFC can introduce small amounts of noise associated with the quantization steps of the current applied to the transverse axes as the reference field changes. Assuming a measurement axis tilt of 3.3°/nT (from Borna, *et al*), these quantization steps correspond to < 0.005° on the transverse axes. Thus, there will be a negligible modulation of effective sensor gain. DFC compensation will also have some dependency on reference sensor noise. However, computing compensation after applying a moderate lowpass filter of, say, 20 Hz, reduces reference component noise while allowing tracking of the typically slow changes in the ambient field. The lowpass filter also serves to attenuate the influence of 60 Hz US power line interference on the compensation components. While our choice of low-pass cutoff appears to capture ambient field fluctuations while suppressing the 27Hz test coil signal, we have not fully explored this parameter space. Likewise, while we chose an exponential moving average filter for simplicity, there may be more robust options that could be explored.

The accuracy of DFC will also be impacted by intrinsic sensor scale errors, D/A converter linearity, crosstalk among sensors, and especially internal crosstalk among the three field-coil pairs. The tests presented in this work were run using nominal closed-loop sensor-gain calibrations. Errors in reference sensor gain calibration may result in incomplete compensation of the transverse fields, and residual CAPE effects for all sensors. We did not account for crosstalk in these measurements. The original FieldLine design anticipated that closed-loop operation would induce crosstalk between the b_Z coils of neighboring sensors, and thus fabricated sensors with self-shielded coils along the sensing axis rather than simple Helmholtz coils to minimize this effect leading to hardware crosstalk of less than 2% in the closest possible packing (Nardelli et al., 2019). Because DFC additionally drives the transverse coils, which do not incorporate shielded coils, additional crosstalk will be induced and may need to be corrected to achieve precision measurements. Currently only crosstalk affecting the b_Z measurements can be empirically evaluated, although expected crosstalk can be derived theoretically.

In this report, we operated all the sensors in closed-loop mode. In closed-loop, no dynamic compensation is used for the b_Z measurement because closed-loop operation already ensures null field in this direction in the cell. Instead, 1st-gradient response for the baselines between the primary sensors in the references were synthesized by digital subtraction in software. It is also possible to obtain intrinsic 1st-gradient response directly, without digital subtraction, by applying compensation to b_Z in open-loop mode dynamically during *acquisition*. This mode of operation, however, will not correct inherent nonlinearities due to the dispersion curve of the sensor response, given that the reference sensors must still function as magnetometers. Furthermore, it presumes that the D/A resolution for b_Z compensation does not add quantization noise.

Compensation methods such as DFC and closed-loop feedback control of field offsets are crucial to accurate brain-source estimation when applying linearly constrained minimum variance (LCMV) beamforming to OPM MEG recordings. Beamforming can be considered as spatially-selective interference attenuation (Sekihara and Nagarajan, 2008). Despite there being an accurate forward model for a given source location, OPM MEG measurement errors will attenuate source strength estimates and can also result in mis-localization of activity in functional brain images (Borna et al., 2021). Simulations have demonstrated that the performance of a similar OPM array to differentiate independent sources using beamforming is degraded for gain errors more than 1-2% (Nugent et al., 2022). Since the sensor array used in these experiments did not have stops to fix the position of the sensors within each slot, only the sensor orientations were precisely known. Measurement of localization errors using a dipole fit were not possible (the ground truth location was unknown).

The cross-axis DFC developed herein can also be applied to other physiological and physical measurements that use OPM sensors, such as magnetocardiography and magnetospinography (Sumiya et al., 2017). The data we present, along with prior studies (Borna et al., 2021; Boto et al., 2017; Iivanainen et al., 2019), have demonstrated that even small deviations from null field within the OPM sensors will introduce significant measurement errors. We show that DFC is remarkably effective at reducing errors due to CAPE and will enable a new frontier of high precision measurements with OPMs.

Data and Code Availability Statement

The Python scripts for implementing dynamic field compensation on the FieldLine OPM electronics are available for download at https://github.com/nih-megcore/OPMLab. These scripts utilize custom APIs and firmware provided by FieldLine Inc. (https://fieldlineinc.com). The OPM data used in these analyses are available upon request from the corresponding author.

Data Availability

Data will be made available on request.

Credit authorship contribution statement

Stephen E. Robinson: Conceptualization, Methodology, Formal analysis, Writing – original draft, Funding acquisition. **Amaia Benitez Andonegui:** Software, Investigation, Data curation, Writing – review & editing. **Tom Holroyd:** Software, Investigation, Data curation, Writing – review & editing. **K. Jeramy Hughes:** Resources, Writing – review & editing. **Orang Alem:** Resources, Writing – review & editing. **Svenja Knappe:** Resources, Writing – review & editing. **Tyler Maydew:** Software. **Andreas Griesshammer:** Software. **Allison Nugent:** Conceptualization, Writing – review & editing, Supervision, Project administration, Funding acquisition.

Acknowledgements

This work was supported by the NIMH Intramural Research Program (1ZICMH002889) and the NIH Brain Initiative (1RO1EB028645). The calibrator electronics and sensor array fixtures were developed in collaboration with the NIMH Section on Instrumentation, including George Dold, Bruce Pritchard, Brian Strempel, and Katherine Cameron.

References

Ahonen, A., Hamalainen, M., Kajola, M., et al., 1992. A 122-channel magnetometer covering the whole head. In: Proceedings of the Satellite Symposium on Neuroscience and Technology. IEEE Transactions on Biomedical Engineering, Lyon, France, pp. 16–20.

Allred, J.C., Lyman, R.N., Kornack, T.W., Romalis, M.V., 2002. High-sensitivity atomic magnetometer unaffected by spin-exchange relaxation. Phys. Rev. Lett. 89, 130301.

Borna, A., Iivanainen, J., Carter, T.R., McKay, J., Taulu, S., Stephen, J., Schwindt, P.D.D., 2021. Cross-axis projection error in optically pumped magnetometers and its implication for magnetoencephalography systems. Neuroimage, 118818.

Boto, E., Holmes, N., Leggett, J., Roberts, G., Shah, V., Meyer, S.S., Munoz, L.D., Mullinger, K.J., Tierney, T.M., Bestmann, S., Barnes, G.R., Bowtell, R., Brookes, M.J., 2018. Moving magnetoencephalography towards real-world applications with a wearable system. Nature 555, 657–661.

Boto, E., Meyer, S.S., Shah, V., Alem, O., Knappe, S., Kruger, P., Fromhold, T.M., Lim, M., Glover, P.M., Morris, P.G., Bowtell, R., Barnes, G.R., Brookes, M.J., 2017. A new generation of magnetoencephalography: room temperature measurements using optically-pumped magnetometers. Neuroimage 149, 404–414.

Boto, E., Shah, V., Hill, R.M., Rhodes, N., Osborne, J., Doyle, C., Holmes, N., Rea, M., Leggett, J., Bowtell, R., Brookes, M.J., 2022. Triaxial detection of the neuromagnetic field using optically-pumped magnetometry: feasibility and application in children. Neuroimage 252, 119027.

Cheyne, D., Vrba, J., Crisp, D., Betts, K., Burbank, M., Cheung, T., Fife, A.A., Haid, G., Kubik, P., Lee, S., McCubbin, J., McKay, J., McKenzie, D., Spear, P., Taylor, B., Tillotson, M., Weinberg, H., Basar, E., Tsutada, T., 1992. Use of an unshielded, 64-channel whole-cortex MEG system in the study of normal and pathological brain function. In: Proceedings of the Satellite Symposium on Neuroscience and Technology. IEEE Engineering in Medicine and Biology, Lyon, France, pp. 46–50.

Cohen, D., 1967. Enhancement of ferromagnetic shielding against low frequency magnetic fields. Appl. Phys. Lett. 10, 67–69.

Cohen, D., 1968. Magnetoencephalography: evidence of magnetic field produced by alpha rhythm currents. Science 161 784-768.

Cohen, D., 1972. Magnetoencephalography: detection of the brain's electrical activity with a superconducting magnetometer. Science 175, 664–666.

Cohen-Tannoudji, C., Dupont-Roc, J., Haroche, S., Laloe, F., 1970. Diverses résonances de croisement de niveaux sur des atomes pompés optiquement en champ nul. I. Théorie. Rev. Phys. Appl. (Paris) 5, 95–101.

Dupont-Roc, J., Haroche, S., Cohen-Tannoudji, C., 1969. Detection of very weak magnetic fields (10-9 gauss) by 87Rb zero-field crossing resonances. Phys. Lett. 28A, 638–639.

Fife, A.A., Vrba, J., Haid, G., Hoang, T., Kubik, P.R., Lee, S., Loewen, R., McKay, J., McKenzie, D., Robinson, S.E., Spear, P., Tillotson, M., Coppola, R., 2002. A 275-channel whole cortex MEG system. In: Nowak, H., Hauesen, J., Gießler, F., Huonker, R. (Eds.), Proceedings of the 13th International Conference on Biomagnetism. VDE Verlag GMBH, Jena, Germany, pp. 912–914.

Hamalainen, M.S., Hari, R., Ilmoniemi, R.J., Knuutila, J., Lounasmaa, O.V., 1993. Mathematical dipoles are adequate to describe realistic generators of human brain activity. Rev. Mod. Phys. 65, 413–498.

Happer, W., Tang, H., 1973. Spin-exchange shift and narrowing of magnetic resonance lines in optically pumped alkali vapors. Phys. Rev. Lett. 31, 273.

Hill, R.M., Devsagaya, J., Holmes, N., Boto, E., Shah, V., Osborbe, J., Safar, K., Worcester, F., Mariani, C., Dawson, E., Woolger, D., Bowtell, R., Taylor, M.J., Brookes, M.J., 2022. Using OPM-MEG in contrasting magnetic environments. Neuroimage 253, 119084.

Holmes, N., Leggett, J., Boto, E., Roberts, G., Hill, R.M., Tierney, T.M., Shah, V., Barnes, G.R., Brookes, M.J., Bowtell, R., 2018. A bi-planar coil system for nulling background magnetic fields in scalp mounted magnetoencephalography. Neuroimage 181, 760–774.

Holmes, N., Tierney, T.M., Leggett, J., Boto, E., Mellor, S., Roberts, G., Hill, R.M., Shah, V., Barnes, G.R., Brookes, M.J., Bowtell, R., 2019. Balanced, bi-planar magnetic field and field gradient coils for field compensation in wearable magnetoencephalography. Sci. Rep. 9, 14196.

Huang, H.C., Dong, H.F., Hu, X.Y., Chen, L., Gao, Y., 2015. Three-axis atomic magnetometer based on spin precession modulation. Appl. Phys. Lett. 107, 182403.

Iivanainen, J., Makinen, A.J., Zetter, R., Stenroos, M., Ilmoniemi, R.J., Parkkonen, L., 2021. Spatial sampling of MEG and EEG based on generalized spatial-frequency analysis and optimal design. Neuroimage 245, 118747.

Iivanainen, J., Zetter, R., Gron, M., Hakkarainen, K., Parkkonen, L., 2019. On-scalp MEG system utilizing an actively shielded array of optically-pumped magnetometers. Neuroimage 194, 244–258.

Kim, K., Begus, S., Xia, H., Lee, S.K., Jazbinsek, V., Trontelj, Z., Romalis, M.V., 2014. Multi-channel atomic magnetometer for magnetoencephalography: a configuration study. Neuroimage 89, 143–151.

Knappe, S., Mhaskar, R., Preusser, J., Kitching, J., Trahms, L., Sander, T., 2012. Chip-scale room- temperature atomic magnetometers for biomedical measurements. In: 5th European Conference of the International Federation for Medical and Biological Engineering, pp. 1330–1333.

Lee, H.J., Shim, J.H., Moon, H.S., Kim, K., 2014. Flat-response spin-exchange relaxation free atomic magnetometer under negative feedback. Opt. Express 22, 19887–19894.

Luessi, M., N, A., Lew, S., Okada, Y., Hamalainen, M., 2014. Performance evaluation of a novel pediatrix MEG system. The 19th International Conference of Biomagnetism pp. P1-002.

Mellor, S., Tierney, T.M., OaNeill, G.C., Alexander, N., Seymour, R.A., Holmes, N., Lopez, J.D., Hill, R.M., Boto, E., Rea, M., Roberts, G., Leggett, J., Bowtell, R., Brookes, M.J., Maguire, E.A., Walker, M.C., Barnes, G.R., 2022. Magnetic field mapping and correction for moving OP-MEG. IEEE Trans. Biomed. Eng. 69, 528–536.

Mellor, S.J., Tierney, T., O'Neill, G., Alexander, N., Seymour, R., Holmes, N., Lopez, J.D., Hill, R., Boto, E., Rea, M., Roberts, G., Leggett, J., Bowtell, R., Brookes, M.J., Maguire, E., Walker, M., Barnes, G., 2021. Magnetic field mapping and correction for moving OP-MEG. IEEE Trans. Biomed. Eng. PP.

Nardelli, N.V., Krzyzewski, S.P., Knappe, S.A., 2019. Reducing crosstalk in optically-pumped magnetometer arrays. Phys. Med. Biol. 64 21NT03.

Nardelli, N.V., Perry, A.R., Krzyzewski, S.P., Knappe, S., 2020. A conformal array of microfabricated optically-pumped first-order gradiometers for magnetoencephalograph. Eur. Phys. J. Quantum Technol. 7.

Nugent, A.C., Andonegui, A.B., Holroyd, T., Robinson, S.E., 2022. On-scalp magnetocorticography with optically pumped magnetometers: simulated performance in resolving simultaneous sources. Neuroimage: Rep. 2, 100093.

Pfeiffer, C., Ruffieux, S., Jönsson, L., Chukharkin, M.L., Kalaboukhov, A., Xie, M., Winkler, D., Schneiderman, J.F., 2020. A 7-channel high-Tc SQUID-based on-scalp MEG system. IEEE Trans. Biomed. Eng. 67, 1483–1489.

Riaz, B., Pfeiffer, C., Schneiderman, J.F., 2017. Evaluation of realistic layouts for next generation on-scalp MEG: spatial information density maps. Sci. Rep. 7, 6974.

Sekihara, K., Nagarajan, R., 2008. Adaptive spatial filters for electromagnetic brain imaging. In: Series in Biomedical Engineering, Berlin, Heidelberg. Springer-Verlag, pp. 72–82.

Shah, V., Knappe, S., Schindt, P.D.D., Kitching, J., 2007. Subpicotesla atomic magnetometry with a microfabricated vapour cell. Nat. Photon. 1, 648–652.

Shah, V.K., Wakai, R.T., 2013. A compact, high performance atomic magnetometer for biomedical applications. Phys. Med. Biol. 58, 8153–8161.

Sumiya, S., Kawabata, S., Hoshino, Y., Adachi, Y., Sekihara, K., Tomizawa, S., Tomori, M., Ishii, S., Sakaki, K., Ukegawa, D., Ushio, S., Watanabe, T., Okawa, A., 2017. Magnetospinography visualizes electrophysiological activity in the cervical spinal cord. Sci. Rep. 7, 2192.

Tierney, T.M., Alexander, N., Mellor, S., Holmes, N., Seymour, R., O'Neill, G.C., Maguire, E.A., Barnes, G.R., 2021. Modelling optically pumped magnetometer interference in MEG as a spatially homogeneous magnetic field. Neuroimage 244, 118484.

Vrba, J., Cheung, T., Taylor, B., Robinson, S.E., 1998. Synthetic higher-order gradiometers reduce environmental noise, not measured brain signals. In: Yoshimoto, T. (Ed.), 17th International Conference Biomagnetism. Tohoku University Press.

Vrba, J., Robinson, S.E., 2000. Linearly constrained minimum variance beamformers, synthetic aperture magnetometry and MUSIC in MEG applications. In: IEEE Proc. 34th Asilomar Conference on Signals, Systems and Computers, Madison, USA, Asilomar, CA. Omnipress, pp. 313–317.

Vrba, J., Robinson, S.E., 2001. Signal processing in magnetoencephalography. Methods 25, 249–271.

Vrba, J., Robinson, S.E., 2002. SQUID sensor array configurations for magnetoencephalography applications. Superconduct. Sci. Technol. 15, R51–R89.

Xia, H., Baranga, A.B.-A., Hoffman, D., Romalis, M.V., 2006. Magnetoencephalography with an atomic magnetometer. Appl. Phys. Lett. 89 211104-211103.

Yan, Y., Lu, J., Zhang, S., Lu, F., Yin, K., Wang, K., Zhou, B., Liu, G., 2022. Three-axis closed-loop optically pumped magnetometer operated in the SERF regime. Opt. Express 30, 18300.